

## Supporting Information for:

# Interlayer Quasi-Bonding Interactions in 2D Layered Materials: A Classification According to the Occupancy of Involved Energy Bands

Yuan-Tao Chen,<sup>1,2,†</sup> Peng-Lai Gong,<sup>1,2,†</sup> Yin-Ti Ren,<sup>2</sup> Liang Hu,<sup>2</sup> Hu Zhang,<sup>1</sup> Jiang-Long Wang,<sup>1</sup> Li Huang,<sup>2,3,\*</sup> and Xing-Qiang Shi<sup>1,\*</sup>

<sup>1</sup>Key Laboratory of Optic-Electronic Information and Materials of Hebei Province, Institute of Life Science and Green Development, College of Physics Science and Technology, Hebei University, Baoding 071002, P. R. China

<sup>2</sup>Department of Physics, Southern University of Science and Technology, Shenzhen 518055, P. R. China

<sup>3</sup>Guangdong Provincial Key Laboratory of Energy Materials for Electric Power, Shenzhen, 518055, P. R. China

<sup>†</sup>These authors contributed equally to this work

\*E-mails: shixq20hbu@hbu.edu.cn, huangl@sustech.edu.cn

## Contents

I. Computational Methods .....	2
II. The frontier orbitals .....	3
III. The test of van der Waals (vdW) correction methods .....	3
IV. The geometric structures .....	4
V. The interlayer couplings .....	6
VI. The SOC and HSE06 calculations .....	7
VII. The Bader charge analysis of monolayer and bilayer arsenene .....	10
VIII. Transition in trilayer arsenene .....	10
IX. The metal-semiconductor transition between single-layer and monolayer SnP <sub>3</sub> .....	11
X. The charge transfer in bilayer SnP <sub>3</sub> .....	13
XI. The Bader charge analysis of monolayer and bilayer SnP <sub>3</sub> .....	14

XII.	The bonding and anti-bonding states in bilayer SnP <sub>3</sub> .....	14
XIII.	The interlayer Sn--Sn interactions.....	15
XIV.	Band evolution of interaction of the interactions of two SnP <sub>3</sub> bilayers .....	16
XV.	Transition between single-layer and monolayer in InP <sub>3</sub> .....	17
XVI.	The interlayer In--In interaction.....	18
XVII.	The Bader charge analysis of monolayer and bilayer InP <sub>3</sub> .....	19
XVIII.	Other typical 2D material as additional examples: black phosphorus (BP), MoS <sub>2</sub> and InSe.....	20
1.	Black phosphorus .....	20
2.	MoS <sub>2</sub> .....	22
3.	InSe.....	22
	References .....	23

## I. Computational Methods

Density functional theory calculations were performed by using the projector augmented wave (PAW)<sup>1</sup> method as implemented in the Vienna *ab initial* simulation package (VASP)<sup>2-4</sup> with the generalized gradient approximation (GGA) for the exchange-correlation functional in the Perdew-Burke-Ernzerhof (PBE) form<sup>5</sup>. The vacuum space was set to exceed 25 Å to ensure that the interactions between periodic images in the slab model are negligible. The k-mesh was set to  $5 \times 5 \times 1$  for 2D triphosphides (SnP<sub>3</sub> and InP<sub>3</sub>) and  $11 \times 11 \times 1$  for arsenene. Geometric structures were optimized with the conjugated gradient method, and the relaxation process was carried out until the forces on each atom were smaller than 0.01 eV/Å. The self-consistent convergence criterion of energy was set to  $10^{-5}$  eV.

To consider the van der Waals interactions, different methods were tested, including the optB86b, optB88<sup>6-7</sup>, PBE+D2<sup>8</sup>, PBE+D3<sup>9</sup> and SCAN+rvv10<sup>10</sup>. The PBE+D3 method offered the best performance when comparing the calculated lattice constants with the experimental ones for the systems we study here [see Section III], and hence the calculation results in this work were based on the geometries relaxed with the PBE+D3 correction. For band structure calculations, the hybrid functional of HSE06 was also considered<sup>11-13</sup>. Our analyses were mainly based on calculations without the hybrid functional except for InP<sub>3</sub> in which HSE06 give a semiconducting character with a small energy gap while PBE give a metallic character. The effect of spin-orbital coupling (SOC) was not

included because the SOC show minor impact for our systems, as both reported in literature<sup>14</sup> and in our test calculations. These details are given in Section V.

For bonding analysis of interlayer interactions, the LOBSTER package<sup>15-18</sup> was used, which gives crystal orbital Hamiltonian population (COHP)<sup>19</sup> via weighting the density of states (DOS) by the corresponding element of the Hamiltonian. In view of crystal orbitals, the bonding states are characterized by a positive overlap population. The off-site element in the corresponding Hamiltonian will then be negative. Thus, in the COHP, the bonding states are represented by a negative sign. To make the COHP plots easier to grasp, minus COHP ( $-COHP$ ) diagrams are plotted, so the bonding states are positive in all the COHP plots.

## II. The frontier orbitals

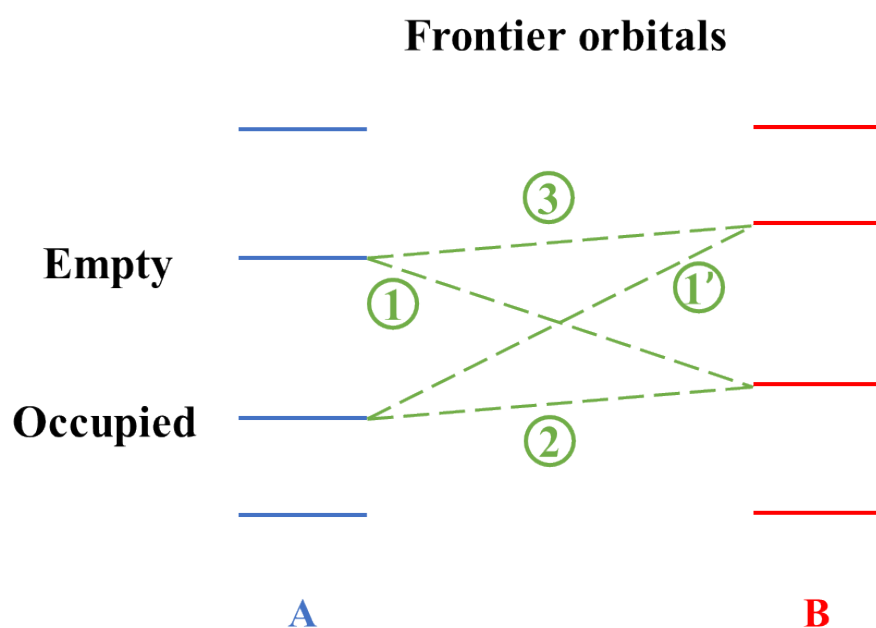


**Figure S1.** The picture of frontier orbitals between molecule/atom A and B. The interactions between these two molecules/atoms could be classified into three types.

The frontier orbital provides a prospective to analyze the interaction from the starting point of the energy levels of the interacting molecules. As the Figure S1 shows, the interaction between A and B could be classified into 3 types according to the total number of electrons in the involved orbitals. The interactions 1 and 1' are stabilizing and the interaction 2 is repulsive because the antibonding goes up

more than the bonding state goes down which raises the total energy. The interaction 3 has no direct energetic consequence because of the unoccupied bonding state.<sup>20</sup>

### III. The test of van der Waals (vdW) correction methods

**Table S1. The relaxed lattice constants of the bulk phase of four 2D materials with various vdW correction methods and the average errors compared with the experimental data.**

		optB86b- vdW-DF	optB88- vdW-DF	PBE+D2	PBE+D3	SCAN+ rvv10	Expt.
Arsenene	a(Å)	3.82	3.83	3.80	3.82	3.78	3.76
	c(Å)	10.37	10.79	10.06	10.30	10.19	10.44 (ref 21)
InP <sub>3</sub>	a(Å)	7.53	7.58	7.47	7.52	7.47	7.45
	c(Å)	10.02	10.21	9.84	9.98	10.00	9.88 (ref 22)
SnP <sub>3</sub>	a(Å)	7.43	7.48	7.39	7.43	7.35	7.38
	c(Å)	10.57	10.83	10.46	10.54	10.74	10.51 (ref 23)
MoS <sub>2</sub>	a(Å)	3.16	5.25	3.18	3.16	3.16	3.16
	c(Å)	12.36	13.94	12.42	12.33	12.47	12.32 (ref 24)
Average error	$\Delta a$	0.87%	17.68%	0.55%	0.86%	0.31%	-
	$\Delta c$	0.72%	5.72%	1.35%	0.65%	1.73%	-

Since we mainly focus on the interlayer interaction along the  $c$  axis, we give priority to the performance of different vdW methods along the  $c$  direction. As shown in Table S1, comparing with the experimental results, the PBE+D3 and optB86b-vdW-DF methods show the minimum error for lattice constant  $c$ , and PBE+D3 shows a slight advantage in the optimized lattice constant  $a$ . Therefore, we chose the PBE+D3 method to handle the vdW correction in the rest of the calculations.

### IV. The geometric structures

Figure S2 shows the monolayer, bilayer and trilayer structures of the three materials. It is worth mentioning that according to a previous study, the bilayer and trilayer systems of arsenene have different stackings<sup>25-26</sup>. Specifically, bilayer arsenene has AB and AA stackings. In our test calculation, the AA stacking are more energetically stable than the AB stacking, which agrees with the previous

study, but the total energies of these two phases are similar (within  $\sim 50$  meV). To compare with the stacking structures of the two triphosphides, we used AB stacking in our discussion. The stacking of bulk arsenic is ABC stacking<sup>21</sup>. Thus, we chose ABC stacking in the discussion of trilayer arsenene.

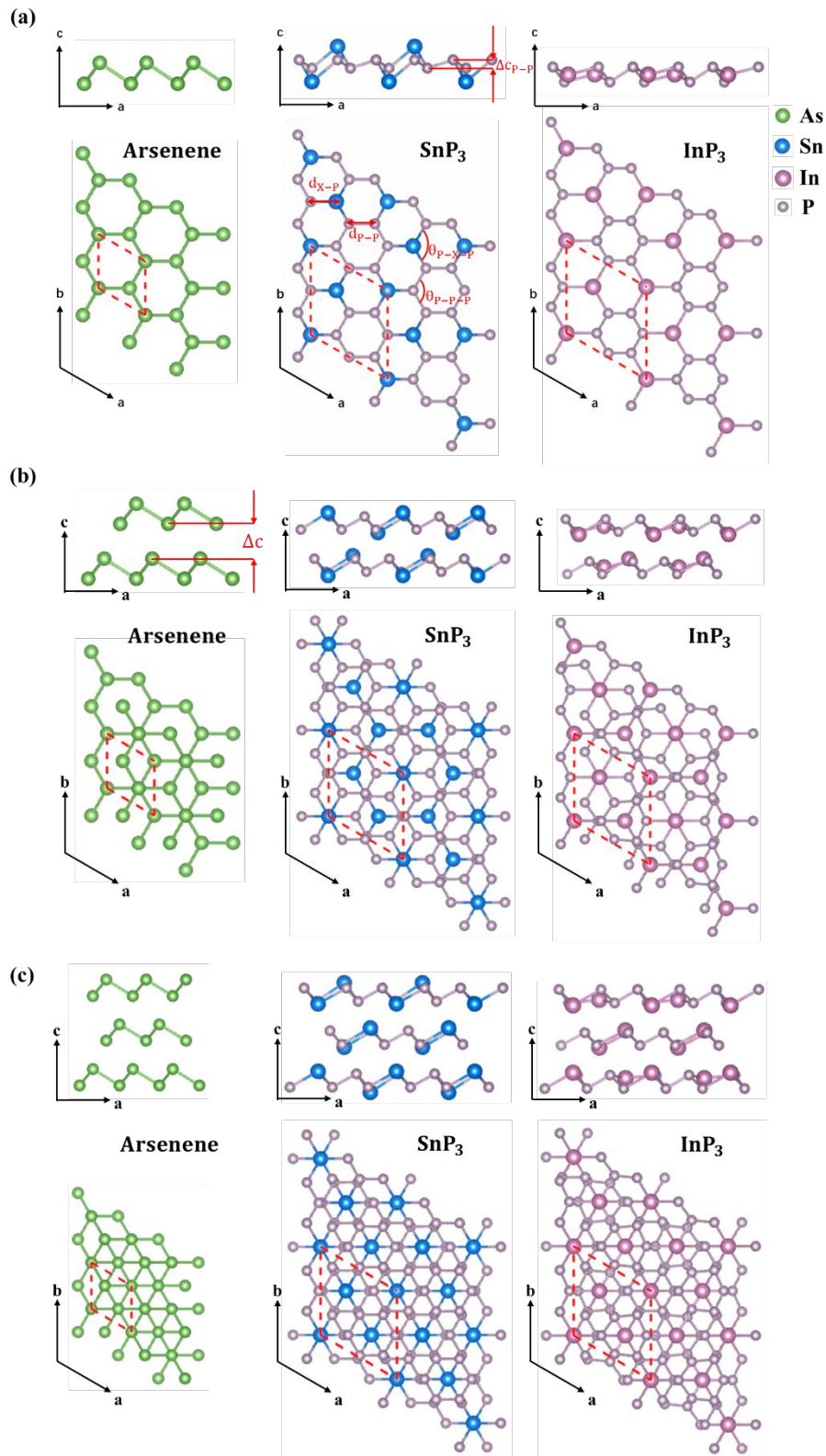


**Figure S2.** The monolayer, bilayer and trilayer structures of the three materials.

**Table S2. Geometrical parameters of one to three layers of arsenene, SnP<sub>3</sub> and InP<sub>3</sub>. N<sub>L</sub> represents the number of layers. *a* is the lattice constants along in-plane direction, and  $\Delta c$  is the interlayer spacing of multilayer system, which is shown in Figure S2b. As shown in Figure S2a,  $d_{p-p}$  represent the bond length between phosphorus atoms (or arsenic atoms in arsenene) and  $d_{x-p}$  are the bond length between X (X = Sn, In) atoms and phosphorus atoms. The two types of  $\theta$  are the corresponding bond angles.**

	N <sub>L</sub>	<i>a</i> (Å)	$\Delta c$ (Å)	$d_{p-p}$ (Å)	$d_{x-p}$ (Å)	$\theta_{p-p-p}$ (°)	$\theta_{p-x-p}$ (°)
Arsenene	1	3.61 (3.60 <sup>24</sup> )	-	2.51 (2.51 <sup>24</sup> )	-	91.99 (91.91 <sup>25</sup> )	-
	2	3.70	2.33	2.53	-	94.14	-
	3	3.73	2.30	2.52	-	95.30	-
SnP <sub>3</sub>	1	7.16 (7.16 <sup>27</sup> ) (7.15 <sup>28</sup> )	-	2.17 (2.171 <sup>27</sup> )	2.71 (2.710 <sup>27</sup> )	111.06 (111.1 <sup>27</sup> )	82.78
	2	7.25 (7.222 <sup>27</sup> ) (7.25 <sup>28</sup> )	1.90 (1.90 <sup>28</sup> )	2.22 (2.218 <sup>27</sup> )	2.62 (2.619 <sup>27</sup> )	96.52 (99.4 <sup>27</sup> )	95.33
	3	7.31 (7.283 <sup>27</sup> ) (7.31 <sup>28</sup> )	2.15 (1.93 <sup>28</sup> )	2.22 (2.227 <sup>27</sup> )	2.65 (2.692 <sup>27</sup> )	97.29 (98.8 <sup>27</sup> )	96.87
InP <sub>3</sub>	1	7.53 (7.557 <sup>29</sup> )	-	2.23 (2.233 <sup>29</sup> )	2.55 (2.580 <sup>29</sup> )	92.89 (92.599 <sup>29</sup> )	114.17
	2	7.47	2.10	2.21	2.55	103.86	97.01
	3	7.48	2.27	2.21	2.67	99.26	100.32

## V. The interlayer couplings

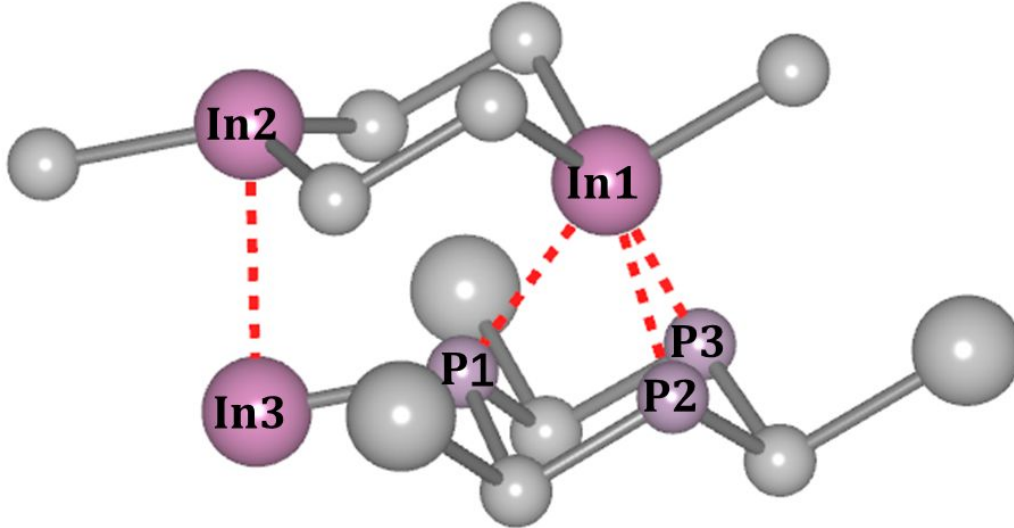


**Figure S3.** The interlayer couplings in  $\text{InP}_3$ . Three interlayer In--P (As--As) interactions (In1--P1, In1--P2 and In1--P3) and one interlayer In--In interaction (In2--In3) are denoted.

We use  $\text{InP}_3$  as an example to explain the interlayer interactions in the three materials we discuss in main text. As Figure S3 shows, there are three X--P (As--As) interlayer interactions in bilayer triphosphides (arsenene). There also exist the interlayer X--X interactions. As the main text describes, we use ‘i’ to indicate the atoms lying in the interlayer region (for example, In1) and ‘o’ to describe another type of atoms (for example, In2 and In3).

## VI. The SOC and HSE06 calculations

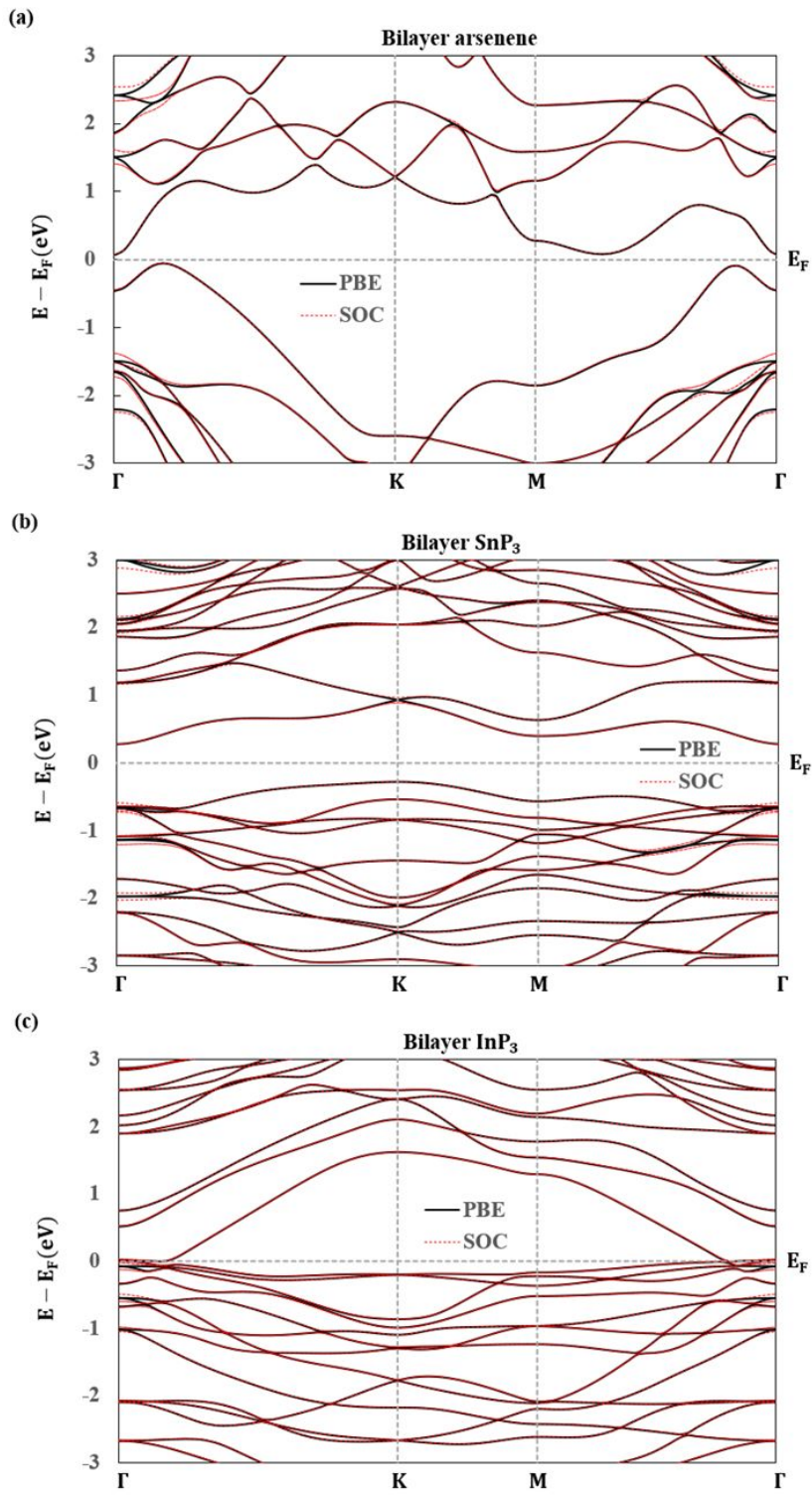


**Figure S4.** The band structures of bilayer Arsenene, bilayer SnP<sub>3</sub> and bilayer InP<sub>3</sub>. The spin-orbital coupling (SOC) has little influence on band gaps and hence does not change our conclusion.

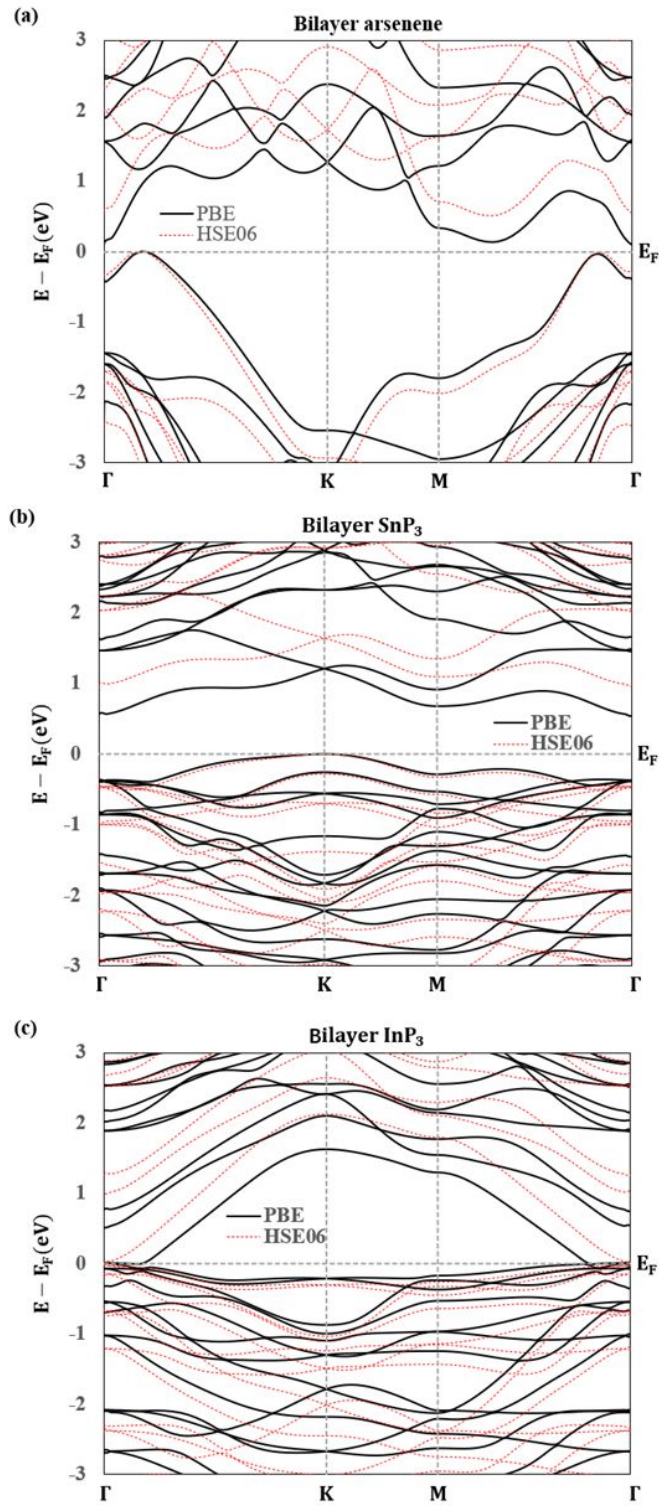


**Figure S5.** The band structures of bilayer Arsenene, bilayer SnP<sub>3</sub> and bilayer InP<sub>3</sub>. The hybrid function has some influence in band gaps.

## VII. The Bader charge analysis of monolayer and bilayer arsenene

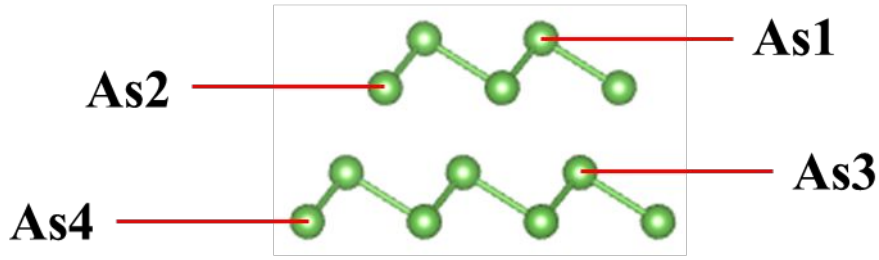


**Figure S6.** The bilayer structure of arsenene. We denote the atoms from top to bottom. For example, As1 denotes the topmost arsenic atoms and As4 denotes the bottommost arsenic atoms.

Figure S6 shows the bilayer arsenene and the symbols we used to denote different atoms in the Bader charge analysis results. Table S3 shows the Bader charge analysis result of monolayer and bilayer. In bilayer, the charge of atoms from the top layer and the atoms from the bottom layer at the similar position are almost the same. Thus, we do not show the Bader charge results of the bottom layer.

**Table S3. The Bader charge analysis result of monolayer and bilayer arsenene.**

	Monolayer	Bilayer
Charge of As1	5.001	5.020
Charge of As2	4.999	4.980

There is no sufficient charge different between the monolayer and bilayer arsenene located in the similar position. It is consistent with our analysis that there is no occupancy change around Fermi level.

## VIII. Transition in trilayer arsenene

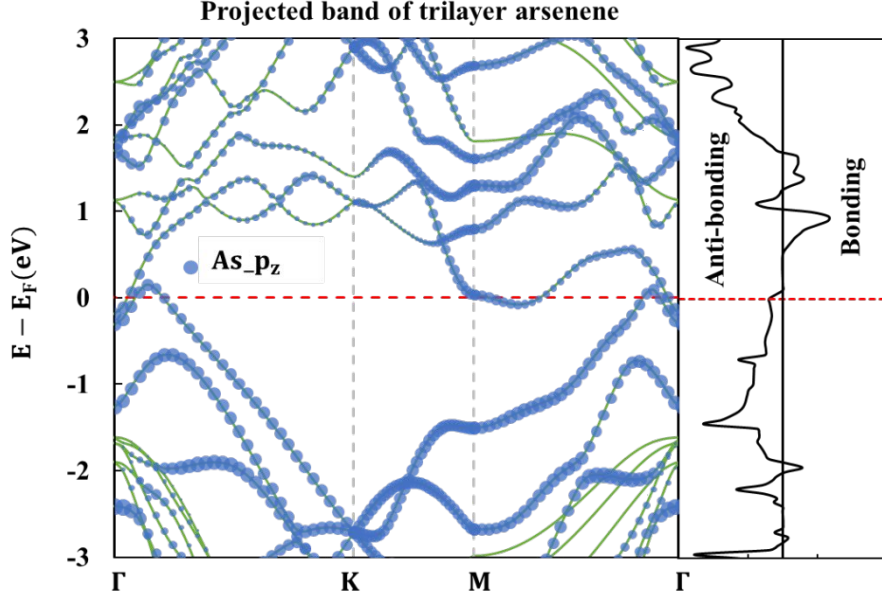


**Figure S7.** The projected band of trilayer arsenene and the pCOHP of interlayer As--As interactions.

As Figure S7 shows, there is a semiconducting-metallic transition from bilayer to trilayer arsenene. According to the pCOHP in the right panel, we could find that the anti-bonding states are still closed to the Fermi level. Although there is a semiconductor-metal transition, this picture is still consistent with our analyses in the main text: the anti-bonding state of the interlayer interaction forms higher energy bands and lifts the VBM in bilayer arsenene. When it comes to trilayer, the higher anti-bonding state is higher than the CBM, so the trilayer arsenene becomes metallic.

## IX. The metal-semiconductor transition between single-layer and monolayer

### $SnP_3$

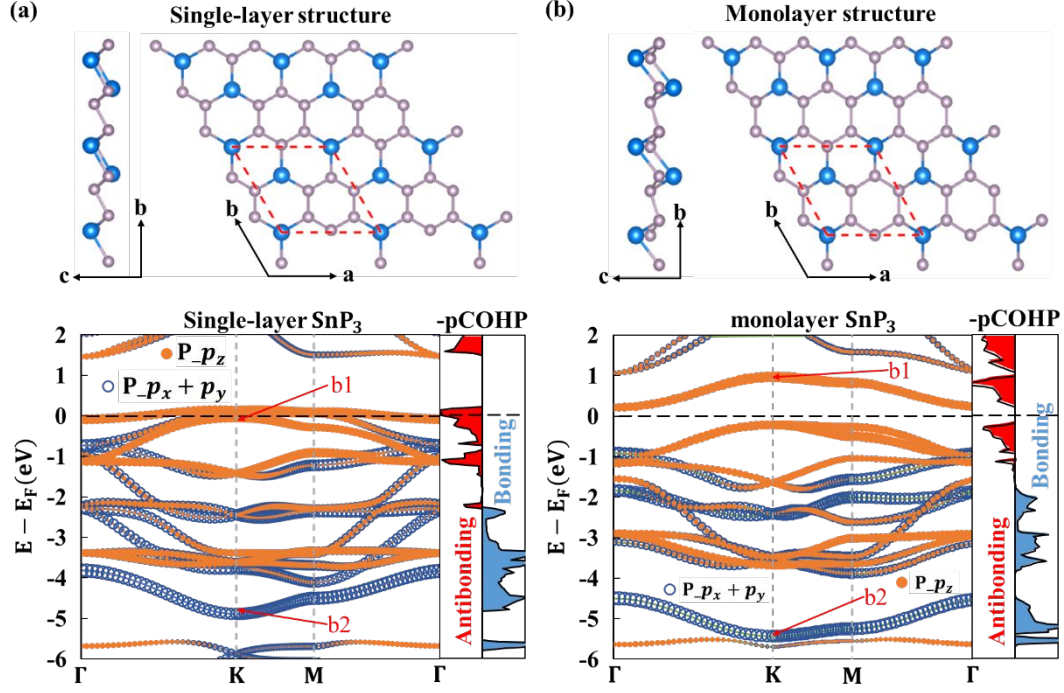


**Figure S8.** The geometric structures (top), projected band structures (bottom) and pCOHPs of intralayer P-P bonds of (a) single-layer and (b) monolayer phases. The bands which play a critical role in the band structure change are denoted as b1 and b2.

As shown in Figure S8, according to the orbital compounds and the similar dispersion of bands, we can relate the corresponding bands between the single-layer and monolayer  $\text{SnP}_3$ . For example, from single-layer to monolayer, the band b1 in the two band structures are both mainly contributed by the  $p_z$  orbital of phosphorus, so we could conclude that the band b1 in monolayer  $\text{SnP}_3$  is come from the band b1 in single-layer  $\text{SnP}_3$ .

The change of these two bands also explains the metal-semiconductor transformation from single-layer to monolayer structure. As Table S4 labels, the monolayer  $\text{SnP}_3$  has shorter intralayer P-P bonds, which lead to a stronger energy level split. Considering the pCOHP of intralayer P-P bonds shown in Figure S8, from single-layer to monolayer  $\text{SnP}_3$ , the shorter P-P bond leads to the higher antibonding state (band b1) and lower bonding state (band b2). The band b1 and b2 are contributed by different orbitals of P atoms due to the hexagonal buckling lattice of geometric structure (refer to Figure S2), but it does not change the conclusion.

**Table S4. Structural parameters in the single-layer and monolayer SnP<sub>3</sub>.** The  $a$  is the lattice constant and  $d$  is bond length, X and P represent the tin and phosphorus atoms, respectively,  $\theta$  is the bond angle,  $\Delta c_{P-P}$  is the separation of phosphorus along the  $c$  axis (as labeled in Figure S2a).

	$a$ (Å)	$d_{P-P}$ (Å)	$d_{X-P}$ (Å)	$\theta_{P-X-P}$ (°)	$\theta_{P-P-P}$ (°)	$\Delta c_{P-P}$ (Å)
Single-layer	7.34	2.22	2.64	97.26	99.21	1.06
monolayer	7.16	2.17	2.70	82.78	111.06	0.66

## X. The charge transfer in bilayer SnP<sub>3</sub>

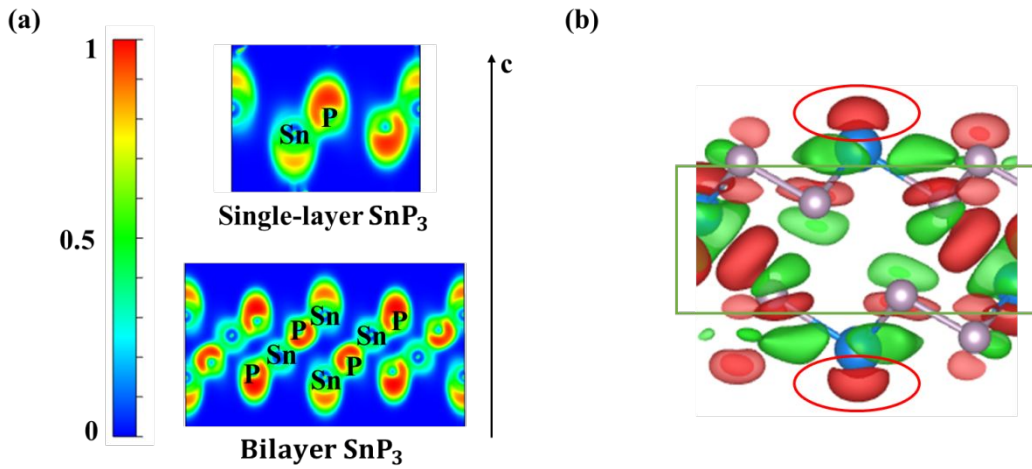


**Figure S9.** The charge transfer from single-layer to bilayer SnP<sub>3</sub>. (a) The electron localization function (ELF) of single-layer and bilayer SnP<sub>3</sub>; (b) The differential charge density of bilayer SnP<sub>3</sub>.

To give an intuitive picture for band structure change between single-layer and bilayer SnP<sub>3</sub>, we take a closer look at the charge distribution of single-layer and bilayer SnP<sub>3</sub> by inspecting the electron localization function (ELF) and the differential charge density. In the ELF, charge localization is shown in red (ELF  $\approx$  1) and the non-local distribution is shown in green (ELF  $\approx$  0.5). The unsaturated orbitals of Sn and the occupied orbitals of P could explain the difference between Sn and P in the ELF plot (Figure S9a, upper panel) of single-layer SnP<sub>3</sub>: the ELF signal of Sn atoms is weaker than that of P atoms. Interestingly, in bilayer SnP<sub>3</sub> (Figure S9a, lower panel), the ELF signal of the outer Sn atoms is enhanced while the signal of Sn atoms at the interlayer region is weakened. It suggests that the outer Sn atoms might have charge accumulation when forming bilayer. The

differential charge density (Figure S9b) confirms this picture. All these are consistent with the band evolution that one of the partially-occupied bands becomes empty and another becomes fully-occupied.

Besides, from Figure S9b, we could also find an electron accumulation in the interlayer region between Sn--P atoms of adjacent layers, which was also reported as a crucial feature of interlayer interaction, but the charge accumulation here is polar instead of typical covalent-like as in other reported materials.<sup>30-32</sup>

## XI. The Bader charge analysis of monolayer and bilayer SnP<sub>3</sub>

**Table S5. The Bader charge analysis results of monolayer and bilayer SnP<sub>3</sub>. The atom1 represents the outmost atoms and atom2 represents the atoms of the interlayer region.**

	Monolayer	Bilayer
Sn1	13.308	13.303
Sn2	13.308	13.082
P1	5.221	5.228
P2	5.230	5.311

Table S5 shows the Bader charge results of monolayer and bilayer. The charge transfer between Sn and P could result for the different electronegativity, which also explains the charge transfer of the interlayer Sn -- P interaction. In the bilayer, the charge of outmost tin atoms is almost unchanged. However, as the Figure S9 shows, to the outmost tin, there are charge depletion along the in-plane direction and charge accumulation along the out-of-plane direction. They increase the occupancy of the out-of-plane orbital (that is, the  $p_z$  orbital) and matches our analysis of band structure change in main text.

## XII. The bonding and anti-bonding states in bilayer SnP<sub>3</sub>

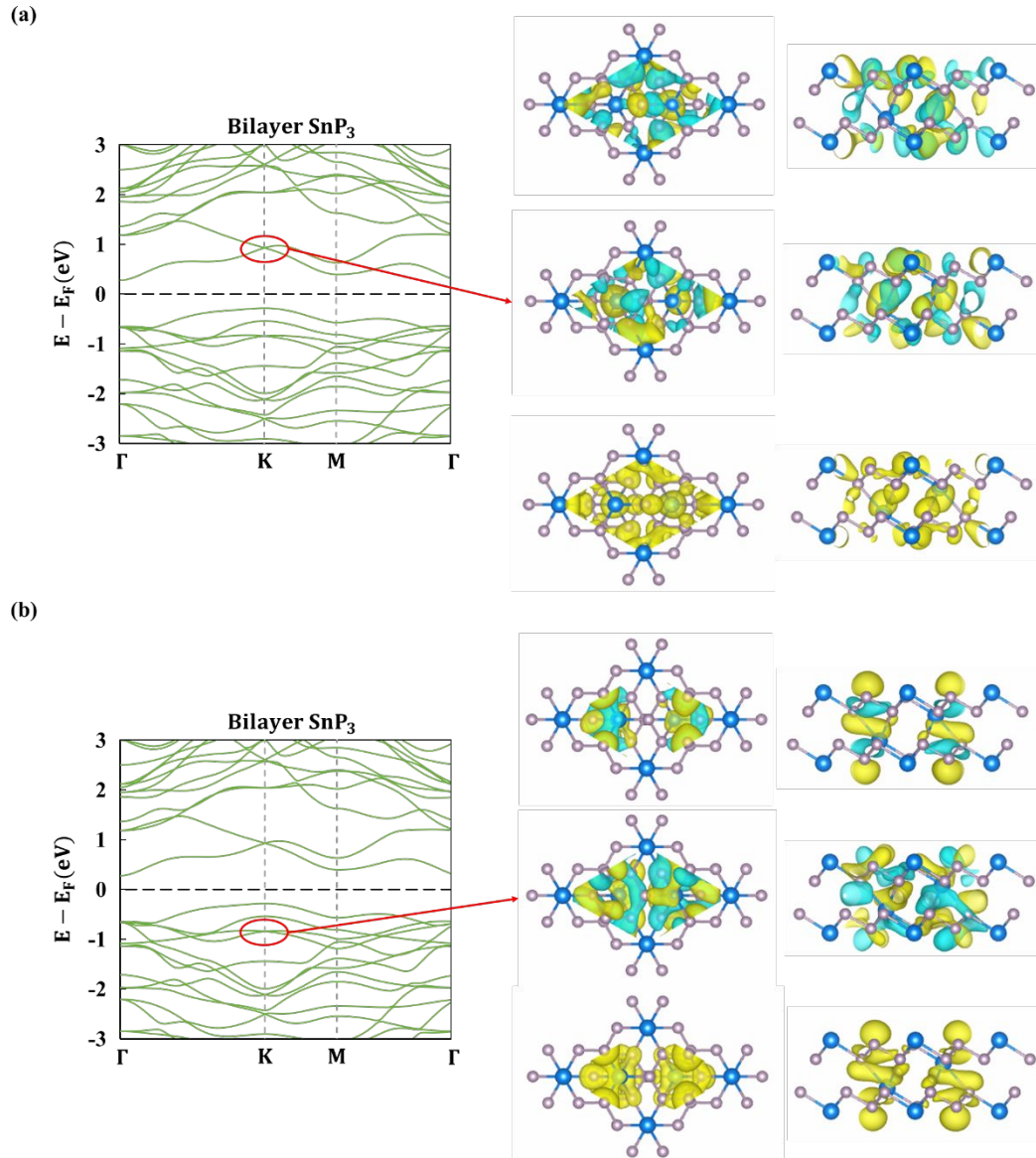


**Figure S10.** The imaginary part (top), real part (middle) of the wavefunction and partial charge density (bottom) of the corresponding k points in certain bands. The interlayer region shows obvious anti-bonding and bonding features in (a) and (b), respectively.

As Figure S10 shows, both the wavefunction and partial charge density plots show bonding and anti-bonding characteristic in the interlayer region. These results confirm that the bands with ellipse are the anti-bonding and bonding states of interlayer Sn--P interactions.

### XIII. The interlayer Sn--Sn interactions

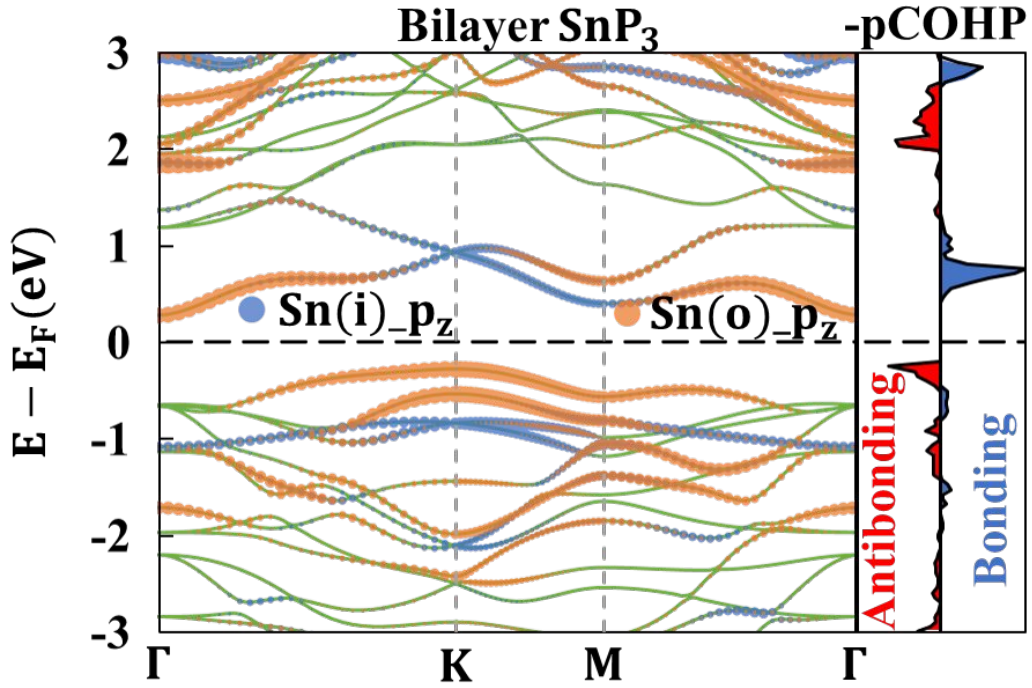


**Figure S11.** The Sn--Sn interlayer interaction in SnP<sub>3</sub>. Projected band structure of bilayer SnP<sub>3</sub> and pCOHP of interlayer Sn--Sn interaction.

As Figure S11 shows, there are interlayer Sn--Sn interaction in bilayer SnP<sub>3</sub>. But this interlayer interaction is weak, it causes the splitting of bVB (antibonding) and bVB-1 (bonding) at K.

#### **XIV. Band evolution of interaction of the interactions of two SnP<sub>3</sub> bilayers**

As we mentioned in the main text, in bilayer, for example, bilayer SnP<sub>3</sub>, the interlayer Sn--P interactions cause the following changes: the bands mainly contributed by the Sn atoms at the interlayer region become empty and the bands mainly contributed by the outmost Sn atoms become fully occupied (refer to Figure 4). Roughly speaking, one group of interlayer Sn--P interactions could cause one partially occupied band (mainly contributed by the out-of-plane orbital of Sn) become empty. In 4L SnP<sub>3</sub>, there are 6 groups of interlayer Sn--P interactions which turn 6 partially occupied bands into empty. Considering the electron conservation, the 2 partially occupied bands contributed by the outmost Sn atoms become fully occupied, and the left electrons occupies the higher energy bands (the degenerate interlayer anti-bonding states) which leads to a semiconductor-metal transition.

Specifically, the bands mainly contributed by the out-of-plane orbitals of the outmost Sn atoms are fully occupied, so the interlayer interaction between two bilayers  $\text{SnP}_3$  could be regarded as the homo-occupancy interaction (interlayer interactions between two fully occupied bands). Thus, the antibonding states could higher the VBM, and possibly induced a semiconductor-metal transition. As Figure S12 shows, the energy bands across Fermi energy are mainly contributed by the Sn atoms of middle interlayer region (which is the interlayer region of two bilayers  $\text{SnP}_3$ ), and the COHP plot suggests that these bands are contributed by the antibonding states of interlayer Sn--P interactions of two bilayers. These results are consistent with our analysis.

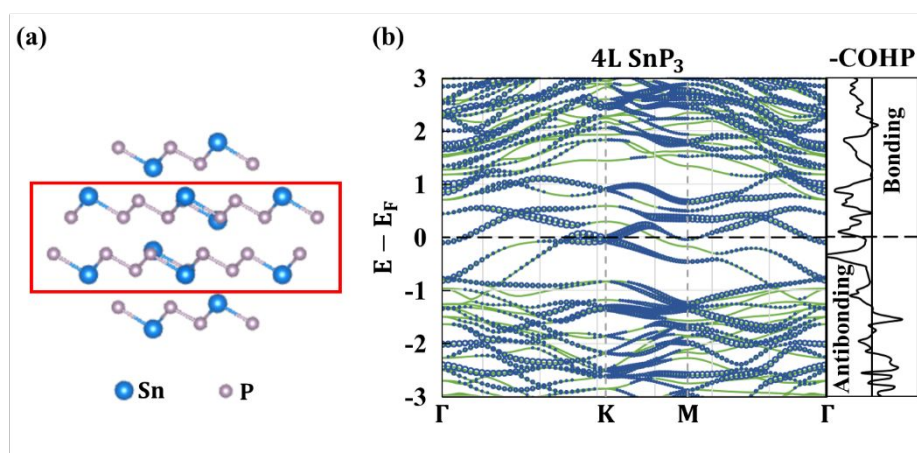


**Figure S12.** The (a) geometric structure and (b) projected band structure of 4L  $\text{SnP}_3$ . The interlayer region of two bilayers is denoted. Here we only project the  $p_z$  orbitals of Sn atoms of middle interlayer region which is the interlayer region of two bilayer  $\text{SnP}_3$ . COHP diagram of the Sn--P interactions in middle interlayer region are plotted.

## XV. Transition between single-layer and monolayer in $\text{InP}_3$

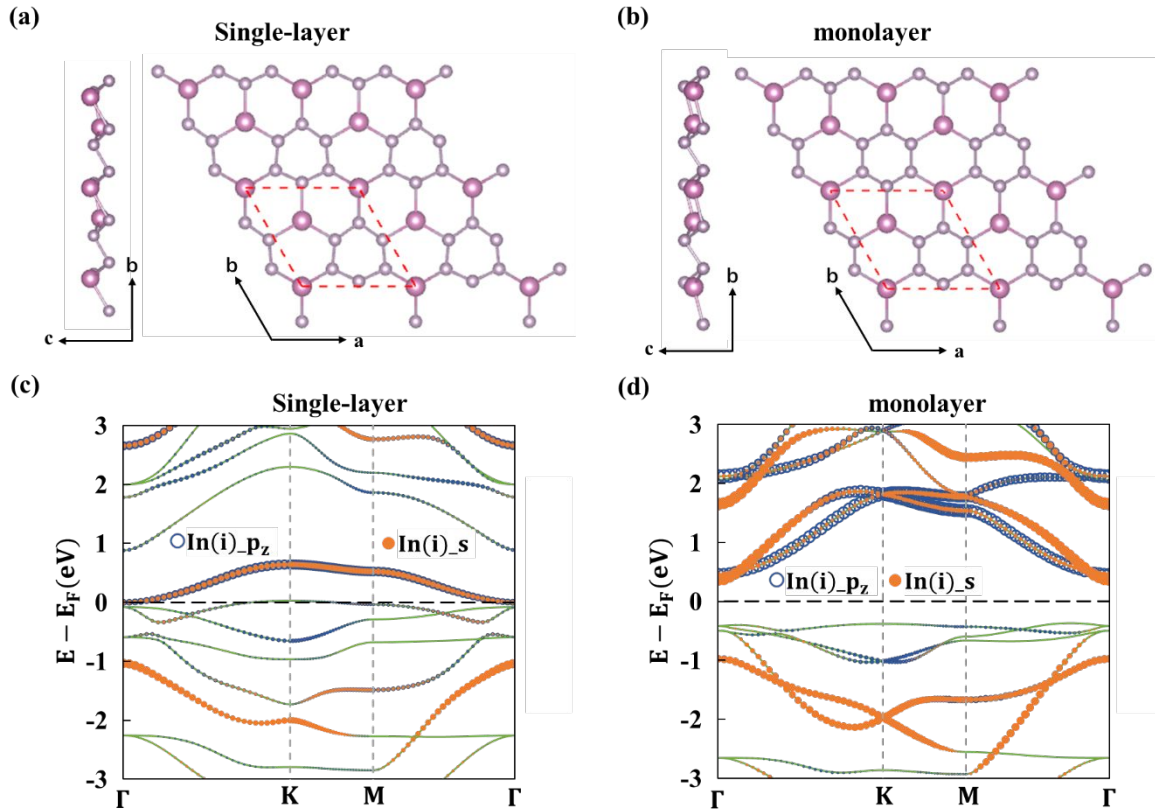


**Figure S13.** Interlayer interaction induced hybridization change in indium and band structure evolution of InP<sub>3</sub>. (a) and (b) Geometric structures of the single-layer (the single-layer from the bilayer) and the monolayer (the original monolayer structure). (c) and (d) The indium *s*- and *p*-orbital projected band structures of the single-layer and monolayer. The ‘i’ denotes the outer indium atoms (corresponding to indium in the interlayer region of bilayer).

As Figure S13b shows, in the semiconducting phase, the  $sp^2$ -like hybridization of indium atoms is mainly in the in-plane directions for the three In-P bonds. Thus, the out-of-plane orbital of indium atoms is empty. The orbitals of phosphorus are fully occupied (like that in the SnP<sub>3</sub>) and the orbitals of indium are fully occupied for in-plane orbitals and empty for out-of-plane orbitals, which causes the semiconducting band structure in Figure S13d. When the  $sp^2$  like hybridization convert into  $sp^3$ -like for the outer indium atom, the vertical orbitals become partially occupied because of the hybridization of 5*s* and 5*p* orbitals of indium, which leads to a metallic band structure with the *s* and *p* hybridized energy bands around the Fermi level, as shown in Figure S13c.

## XVI. The interlayer In--In interaction

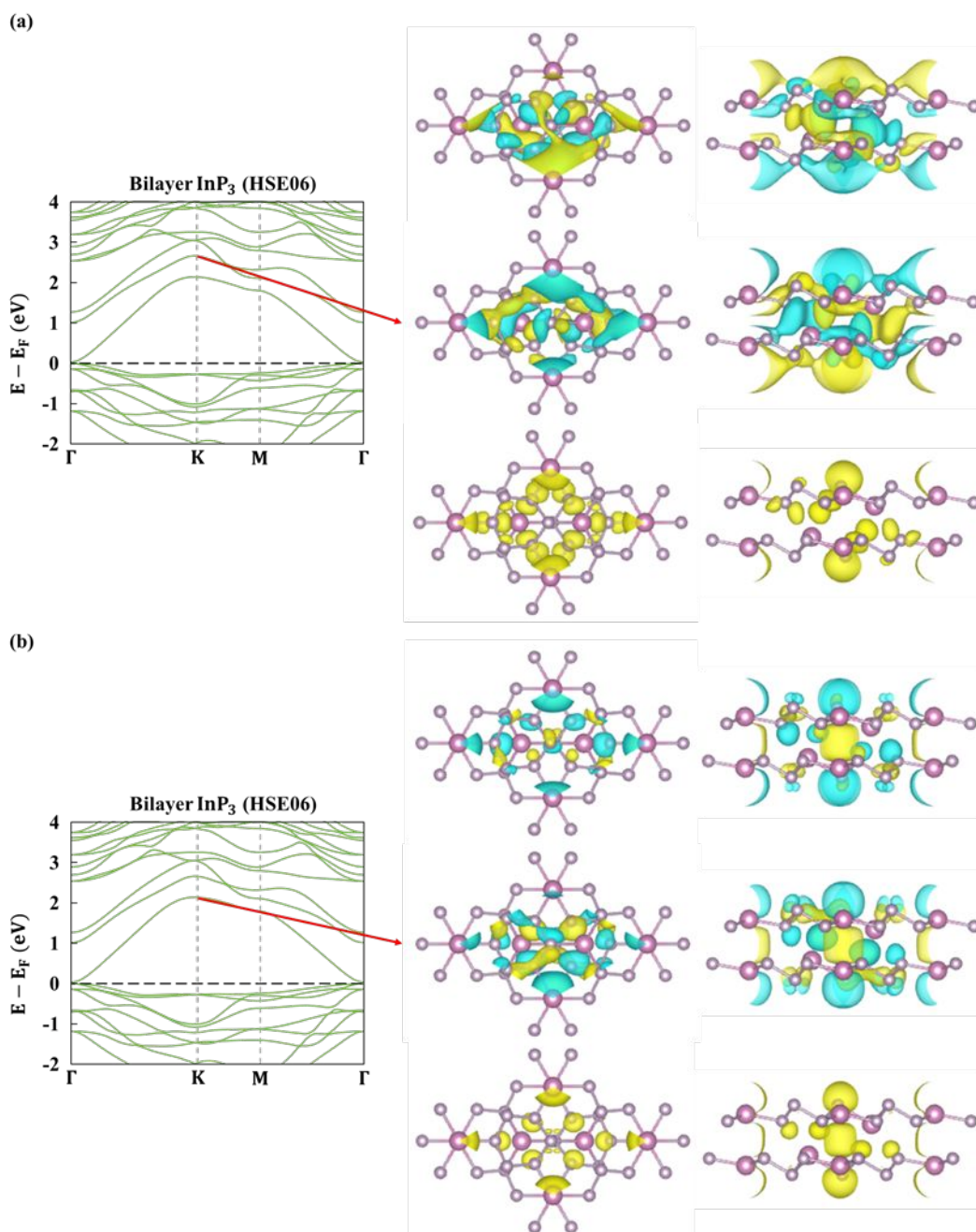


**Figure S14.** The interlayer In--In interaction. The imaginary part (top), real part (middle) of the wavefunction and partial charge density (bottom) of the corresponding k points in certain bands. The interlayer region shows obvious anti-bonding and bonding features in (a) and (b), respectively.

## XVII. The Bader charge analysis of monolayer and bilayer InP<sub>3</sub>

**Table S6. The Bader charge analysis results of monolayer and bilayer InP<sub>3</sub>. The atom1 represents the outmost atoms and atom2 represents the atoms of the interlayer region.**

	Monolayer	Bilayer
In1	12.261	12.266
In2	12.260	12.168
P1	5.250	5.190
P2	5.242	5.327

Here, as we analyzed in the main text, there is no sufficient charge transfer between monolayer and bilayer InP<sub>3</sub>. Also, the difference of charge in monolayer and bilayer P2 could be results for the different electronegativity between In and P.

## **XVIII. Other typical 2D material as additional examples: black phosphorus (BP),**

### **MoS<sub>2</sub> and InSe**

#### **1. Black phosphorus**

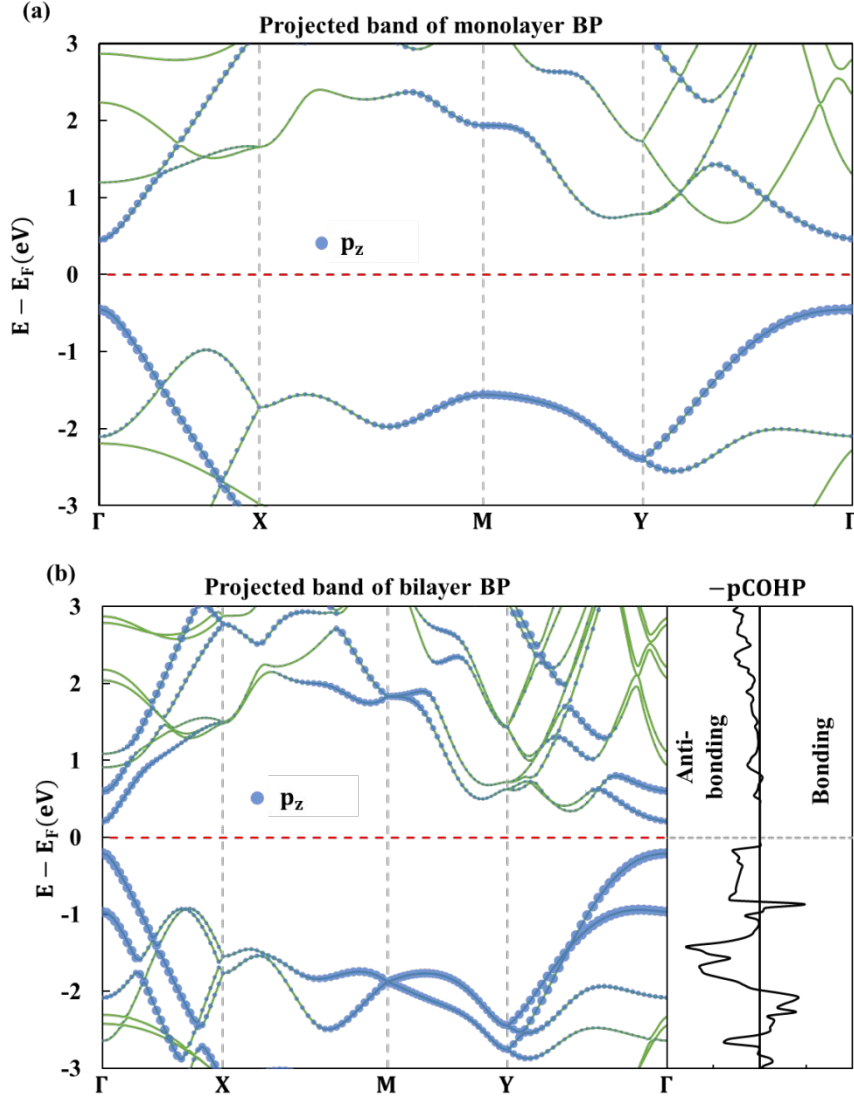


**Figure S15.** (a) Projected band structure of monolayer black phosphorus. The blue part represents the  $p_z$  orbitals of phosphorus. (b) Projected band structure of bilayer black phosphorus. The COHP corresponds the interlayer P--P interactions. The band structures are calculated in PBE and fit well of the previous study<sup>33-34</sup>. The Fermi level is set to zero.

As Figure S15 shows, the band structure change from monolayer BP to bilayer BP is in consistent with our analyses in the main text. The VBM in bilayer BP is mainly contributed by  $p_z$  orbitals and, according to the pCOHP of right panel, it is the anti-bonding states of the interlayer P--P interactions. It suggests that, when two monolayer BP stack to form bilayer, the  $p_z$  orbitals interact and form anti-bonding states which shift up the VBM of bilayer BP. This picture is similar to that in arsenene and fit well with the previous research.<sup>35</sup>

## 2. MoS<sub>2</sub>

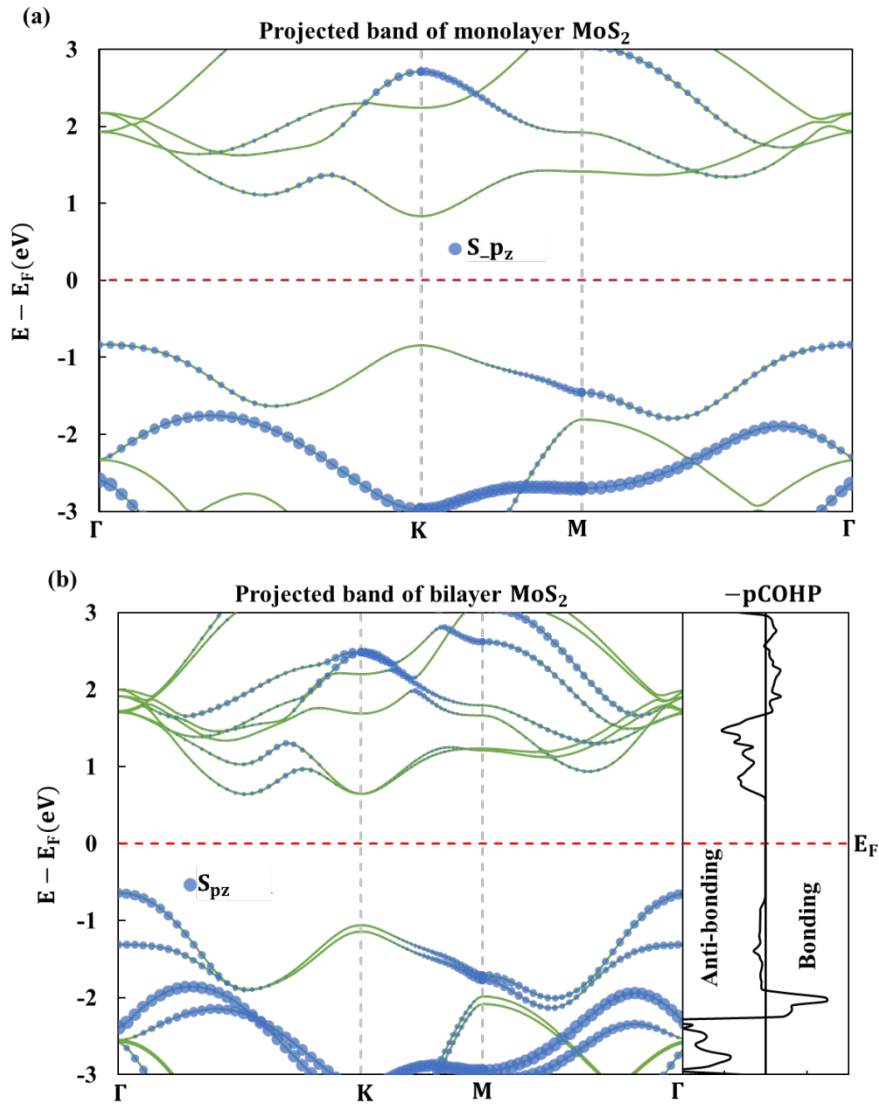


**Figure S16.** (a) Projected band of monolayer MoS<sub>2</sub>. (b) Projected band of bilayer MoS<sub>2</sub>. The COHP corresponds the interlayer S-S interactions.

In bilayer MoS<sub>2</sub>, we could find that the anti-bonding states are no longer being the VBM of bilayer system. However, it does not change our conclusions in the main text. Because the interlayer interaction in MoS<sub>2</sub> is too weak, the anti-bonding states of interlayer S-S is not at the VMB position but near the bands below the Fermi level at around -2eV (Figure S16). This result is in good agreement with the previous study.<sup>31</sup> Besides, the band structure direct-indirect evolution of few-layer MoS<sub>2</sub> is also related to the interlayer interaction.<sup>36</sup>

## 3. InSe

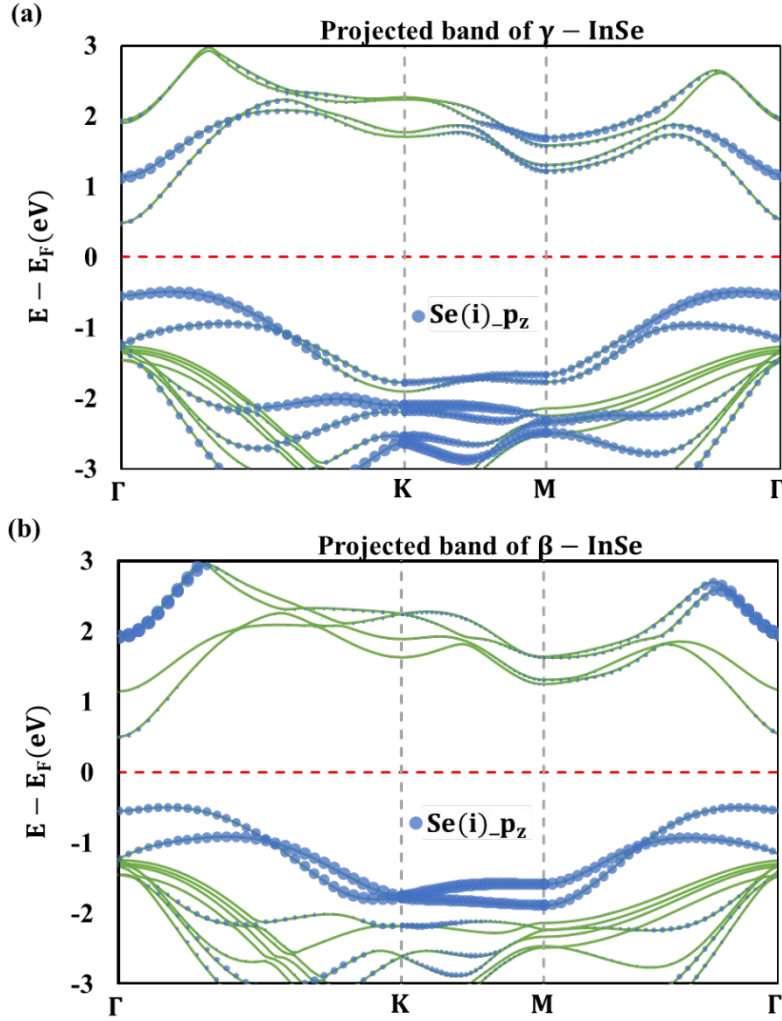


**Figure S17.** Projected energy bands of bilayer (a)  $\gamma$  – InSe and (b)  $\beta$  – InSe.

According to the previous research of Sun *et al.*<sup>37</sup>, both the band structures of the two phases ( $\gamma$  – and  $\beta$  – InSe) of few-layer InSe change as the layer increasing, and the decline of the band gaps are mainly contributed by the rise of VBM. As Figure S17 shows, both the VBM of bilayer  $\gamma$  – and  $\beta$  – InSe are contributed by the  $p_z$  orbitals of Se atoms in the interlayer region. Considering the  $p_z$  orbitals of Se atoms are fully occupied, the interlayer interaction could be classified as the occupied-occupied interactions which will higher the VBM.

## References

- (1) Kresse, G.; Joubert, D. From Ultrasoft Pseudopotentials to the Projector Augmented-Wave Method. *Phys. Rev. B* **1999**, *59*, 1758-1775.
- (2) Kresse, G. Ab Initio Molecular Dynamics for Liquid Metals. *Journal of Non-Crystalline Solids* **1995**, *192-193*, 222-229.
- (3) Kresse, G.; Hafner, J. Ab Initio Molecular-Dynamics Simulation of the Liquid-Metal--Amorphous-Semiconductor Transition in Germanium. *Phys. Rev. B* **1994**, *49*, 14251-14269.
- (4) Kresse, G.; Furthmüller, J. Efficient Iterative Schemes for Ab Initio Total-Energy Calculations Using a Plane-Wave Basis Set. *Phys. Rev. B* **1996**, *54*, 11169-11186.
- (5) Perdew, J. P.; Burke, K.; Ernzerhof, M. Generalized Gradient Approximation Made Simple *Phys. Rev. Lett.* **1997**, *78*, 1396-1396.
- (6) Klimeš, J.; Bowler, D. R.; Michaelides, A. Chemical Accuracy for the van der Waals Density Functional. *Journal of Physics: Condensed Matter* **2009**, *22*, 022201.
- (7) Klimeš, J.; Bowler, D. R.; Michaelides, A. Van der Waals Density Functionals Applied to Solids. *Phys. Rev. B* **2011**, *83*, 195131.
- (8) Bučko, T.; Hafner, J.; Lebègue, S.; Ángyán, J. G. Improved Description of the Structure of Molecular and Layered Crystals: Ab Initio DFT Calculations with van der Waals Corrections. *The Journal of Physical Chemistry A* **2010**, *114*, 11814-11824.
- (9) Grimme, S.; Antony, J.; Ehrlich, S.; Krieg, H. A Consistent and Accurate ab Initio Parametrization of Density Functional Dispersion Correction (DFT-D) for the 94 Elements H-Pu. *The Journal of Chemical Physics* **2010**, *132*, 154104.
- (10) Peng, H.; Yang, Z.-H.; Perdew, J. P.; Sun, J. Versatile van der Waals Density Functional Based on a Meta-Generalized Gradient Approximation. *Physical Review X* **2016**, *6*, 041005.
- (11) Li, Y.; Yang, S.; Li, J. Modulation of the Electronic Properties of Ultrathin Black Phosphorus by Strain and Electrical Field. *The Journal of Physical Chemistry C* **2014**, *118*, 23970-23976.
- (12) Heyd, J.; Scuseria, G. E.; Ernzerhof, M. Hybrid Functionals Based on A Screened Coulomb Potential. *The Journal of Chemical Physics* **2003**, *118*, 8207-8215.
- (13) Krukau, A. V.; Vydrov, O. A.; Izmaylov, A. F.; Scuseria, G. E. Influence of the Exchange Screening Parameter on the Performance of Screened Hybrid Functionals. *The Journal of Chemical Physics* **2006**, *125*, 224106.
- (14) Ersan, F.; Aktürk, E.; Ciraci, S. Stable Single-Layer Structure of Group-V Elements. *Phys. Rev. B* **2016**, *94*, 245417.
- (15) Maintz, S.; Deringer, V. L.; Tchougréeff, A. L.; Dronskowski, R. LOBSTER: A tool to extract chemical bonding from plane-wave based DFT. *Journal of Computational Chemistry* **2016**, *37*, 1030-1035.
- (16) Maintz, S.; Deringer, V. L.; Tchougréeff, A. L.; Dronskowski, R. Analytic Projection from Plane-Wave and PAW Wavefunctions and Application to Chemical-bonding Analysis in Solids. *Journal of Computational Chemistry* **2013**, *34*, 2557-2567.
- (17) Deringer, V. L.; Tchougréeff, A. L.; Dronskowski, R. Crystal Orbital Hamilton Population (COHP) Analysis As Projected from Plane-Wave Basis Sets. *The Journal of Physical Chemistry A* **2011**, *115*, 5461-5466.
- (18) Maintz, S.; Esser, M.; Dronskowski, R. EFFICIENT ROTATION OF LOCAL BASIS FUNCTIONS USING REAL SPHERICAL HARMONICS. *Acta Phys. Pol. B* **2016**, *47*, 1165-1175.

- (19) Dronskowski, R.; Bloechl, P. E. Crystal Orbital Hamilton Populations (COHP): Energy-Resolved Visualization of Chemical Bonding in Solids based on Density-Functional Calculations. *The Journal of Physical Chemistry* **1993**, *97*, 8617-8624.
- (20) Hoffmann, R. *Solids and Surfaces: A Chemist's View of Bonding in Extended Structures*. VCH: New York, 1988.
- (21) Schiferl, D.; Barrett, C. S. The Crystal Structure of Arsenic at 4.2, 78 and 299 DegreesK. *J Appl Crystallogr* **1969**, *2*, 30-36.
- (22) Kinomura, N.; Terao, K.; Kikkawa, S.; Horiuchi, H.; Koizumi, M.; Setoguchi, H. Synthesis and Crystal Structure of InP<sub>3</sub>. *Mater Res Bull* **1983**, *18*, 53-57.
- (23) Gullman, J.; Olofsson, O. The Crystal Structure of SnP<sub>3</sub> and a Note on the Crystal Structure of GeP<sub>3</sub>. *J Solid State Chem* **1972**, *5*, 441-445.
- (24) Petkov, V.; Billinge, S. J. L.; Larson, P.; Mahanti, S. D.; Vogt, T.; Rangan, K. K.; Kanatzidis, M. G. Structure of Nanocrystalline Materials Using Atomic Pair Distribution Function Analysis: Study of LiMoS<sub>2</sub>. *Phys. Rev. B* **2002**, *65*, 092105.
- (25) Kecik, D.; Durgun, E.; Ciraci, S. Stability of Single-Layer and Multilayer Arsenene and Their Mechanical and Electronic Properties. *Phys. Rev. B* **2016**, *94*, 205409.
- (26) Kecik, D.; Durgun, E.; Ciraci, S. Optical Properties of Single-Layer and Bilayer Arsenene Phases. *Phys. Rev. B* **2016**, *94*, 205410.
- (27) Sun, S.; Meng, F.; Wang, H.; Wang, H.; Ni, Y. Novel Two-Dimensional Semiconductor SnP<sub>3</sub>: High Stability, Tunable Bandgaps and High Carrier Mobility Explored Using First-Principles Calculations. *J. Mater. Chem. A* **2018**, *6*, 11890-11897.
- (28) Gong, P.-L.; Zhang, F.; Huang, L.-F.; Zhang, H.; Li, L.; Xiao, R.-C.; Deng, B.; Pan, H.; Shi, X.-Q. Multifunctional Two-Dimensional Semiconductors SnP<sub>3</sub>: Universal Mechanism of Layer-Dependent Electronic Phase Transition. *Journal of Physics: Condensed Matter* **2018**, *30*, 475702.
- (29) Miao, N.; Xu, B.; Bristowe, N. C.; Zhou, J.; Sun, Z. Tunable Magnetism and Extraordinary Sunlight Absorbance in Indium Triphosphide Monolayer. *J. Am. Chem. Soc.* **2017**, *139*, 11125-11131.
- (30) Qiu, X.; Ji, W. Illuminating Interlayer Interactions. *Nat. Mater.* **2018**, *17*, 211-213.
- (31) Zhao, Y.; Qiao, J.; Yu, P.; Hu, Z.; Lin, Z.; Lau, S. P.; Liu, Z.; Ji, W.; Chai, Y. Extraordinarily Strong Interlayer Interaction in 2D Layered PtS<sub>2</sub>. *Adv. Mater.* **2016**, *28*, 2399-2407.
- (32) Kasai, H.; Tolborg, K.; Sist, M.; Zhang, J.; Hathwar, V. R.; Filsø, M. Ø.; Cenedese, S.; Sugimoto, K.; Overgaard, J.; Nishibori, E.; Iversen, B. B. X-ray Electron Density Investigation of Chemical Bonding in van der Waals Materials. *Nat. Mater.* **2018**, *17*, 249-252.
- (33) Qiao, J.; Kong, X.; Hu, Z.-X.; Yang, F.; Ji, W. High-mobility Transport Anisotropy and Linear Dichroism in Few-Layer Black Phosphorus. *Nat. Commun.* **2014**, *5*, 4475.
- (34) Çakır, D.; Sevik, C.; Peeters, F. M. Significant Effect of Stacking on the Electronic and Optical Properties of Few-Layer Black Phosphorus. *Phys. Rev. B* **2015**, *92*, 165406.
- (35) Wang, V.; Liu, Y. C.; Kawazoe, Y.; Geng, W. T. Role of Interlayer Coupling on the Evolution of Band Edges in Few-Layer Phosphorene. *The Journal of Physical Chemistry Letters* **2015**, *6*, 4876-4883.
- (36) Padilha, J. E.; Peelaers, H.; Janotti, A.; Van de Walle, C. G. Nature and Evolution of the Band-Edge States in MoS<sub>2</sub>: From Monolayer to Bulk. *Phys. Rev. B* **2014**, *90*, 205420.

(37) Sun, Y.; Luo, S.; Zhao, X.-G.; Biswas, K.; Li, S.-L.; Zhang, L. InSe: A Two-Dimensional Material with Strong Interlayer Coupling. *Nanoscale* **2018**, *10*, 7991-7998.